Applied Surface Science 466 (2019) 525–534

Contents lists available at ScienceDirect

Applied Surface Science

journal homepage: www.elsevier.com/locate/apsusc

Full Length Article

In-situ preparation of NH_2-MIL-125(Ti)/BiOCl composite with accelerating charge carriers for boosting visible light photocatalytic activity

Qingsong Hu[a,b], Jun Di[b], Bin Wang[b], Mengxia Ji[b], Yong Chen[b], Jiexiang Xia[b,*], Huaming Li[b], Yaping Zhao[a,*]

[a] School of Ecological and Environmental Science, Shanghai Key Laboratory for Urban Ecological Processes and Eco-Restoration, Institute of Eco-Chongming, East China Normal University, Shanghai 200241, PR China
[b] School of Chemistry and Chemical Engineering, Institute for Energy Research, Jiangsu University, 301 Xuefu Road, Zhenjiang 212013, PR China

ARTICLE INFO

Keywords:
Metal-organic frameworks
BiOCl nanosheets
Charges migration
Photocatalysis
Visible light irradiation

ABSTRACT

Metal-organic frameworks (MOFs), a new class of porous and crystalline materials, which have drawn increasing attention in diverse areas. The development of highly active MOFs-based photocatalysts have become a research hotspot owing to the tunable semiconducting properties and highly porous nanostructure. The unique roles of photocatalysis by MOFs can be conventionally optimized towards addressing the environment and energy issues. In this paper, NH_2-MIL-125(Ti)/BiOCl composite was studied as a novel visible-light responsive photocatalyst for the removal of organic contaminants. The composite displays significantly enhanced photocatalytic activity for contaminant degradation as compared with BiOCl and NH_2-MIL-125(Ti), and the optimal NH_2-MIL-125(Ti) content is 10 wt%. The remarkable enhancement of the photocatalytic performance can be ascribed to the absorption of visible-light as well as the efficient charge separation and transfer on the interface contact between BiOCl and NH_2-MIL-125(Ti). Superoxide radicals and holes were determined to be the main active species in the photocatalytic process via the reactive species trapping experiments and electron spin resonance, and the plausible photocatalytic mechanism is presented. This work aims to provide guidelines for developing more organic-inorganic hybrid materials for environmental remediation.

1. Introduction

Photocatalysis, an environmentally friendly technology, can remedy the environment by employing solar energy [1–4]. By far, a lot of research has focused on semiconductor-based photocatalysts, for instance, elemental photocatalysts [5], (oxy)nitrides [6], oxides [7], and plasmonic photocatalysts [8]. Among all the catalysts, bismuth oxychloride (BiOCl) displays a typical tetragonal matlockite structure, in which a $[Bi_2O_2]$ slab is interleaved by double slabs of chlorine in the crystal [9–11]. The unique layered structure provides sufficient space to polarize the interrelated orbitals and atoms to form static electric fields perpendicular to the $[Bi_2O_2]$ and $[Cl_2]$ slices [12,13]. Consequently, the formed static electric fields can promote the effective separation of photogenerated electron-hole pairs, resulting in a preferable photocatalytic performance [14]. Nevertheless, the wide energy band structure of BiOCl causes the absorption of ultraviolet light, leading to a slight solar-light photocatalytic performance due to its inefficient utilization of visible light. Various attempts have been made to increase the visible light response in order to improve the photocatalytic efficiency of BiOCl. Most of them centered on constructing heterogeneous structure [15–17], tailoring size and morphology [18,19] and doping of Br^- or I^- in place of Cl^- ions [20]. Besides, grafting of photosensitizers [21] and surface depositing of metal nanoparticles [22] to obtain visible-light photocatalysis have also been attempted. However, the modified BiOCl photocatalyst does not satisfy the requirements of large-scale practical applications. As a result, it is urgent to design a semiconductor material with high visible-light response and appropriate band-gap structure, and compound it with BiOCl to improve the photocatalytic performance.

Metal-organic frameworks (MOFs), an intriguing family of inorganic-organic hybrid material, are comprised of metal clusters or inorganic metal ions linked by organic bridging ligands via the coordination bonds [23]. MOFs serve as adsorbents [23], catalysts [24], separations [25] and drug delivery agents [26], thanks to their large internal surface area, easy tunability of shape, and a wide diversity of metallic centers. Additionally, MOFs have shown great potential for photocatalysis because of their unique porous structure together with ample physicochemical characteristics of the organic ligands and metal

* Corresponding authors.
E-mail addresses: xjx@ujs.edu.cn (J. Xia), ypzhao@des.ecnu.edu.cn (Y. Zhao).

https://doi.org/10.1016/j.apsusc.2018.10.020
Received 26 July 2018; Received in revised form 29 September 2018; Accepted 3 October 2018
Available online 06 October 2018
0169-4332/

centers [27]. Particularly for NH_2-MIL-125(Ti), a type of amine-functionalized NH_2-Ti-MOF, has been investigated as a visible-light photocatalyst for water purification [28], hydrogen production [29], CO_2 reduction [30] and organic synthesis [31]. Upon illumination, the photogenerated electrons can migrate to the titanium-oxo cluster of NH_2-MIL-125(Ti) through a linker-to-metal charge transfer mechanism (LMCT), which are favored for photocatalysis [32]. In addition, the integration of MOFs with other functional semiconductor materials has achieved the desired photocatalytic characteristics [33]. The large specific surface area, wide visible-light absorption and adjustable band gap edges could be the key properties for improving the photocatalytic performance of traditional inorganic semiconductors.

In this work, we demonstrate one-pot hydrothermal strategy for the preparation of NH_2-MIL-125(Ti)/BiOCl composite with regulable NH_2-MIL-125(Ti) loading amount to enhance the photocatalytic degradation of tetracycline hydrochloride (TC) and bisphenol A (BPA). The characterizations of FTIR, Raman, XPS, TGA and TEM confirm the fabrication of NH_2-MIL-125(Ti)/BiOCl composite, and the degradation results demonstrate that the synthesized composite displays higher photocatalytic activity than pure BiOCl or NH_2-MIL-125(Ti). The mechanism underlying the contaminants photodegradation in this work is studied via electron spin resonance (ESR) analysis and reactive species trapping experiments. Our findings offers a vital insight into the designing of organic-inorganic composite photocatalysts with outstanding performance and improved stability for the application in environmental purification.

2. Experimental

2.1. Materials

All chemicals used in this experiment were analytical grade purity without further purification. The ionic liquid [C_{16}mim]Cl (1-hexadecyl-3-methylimidazolium chloride) was purchased from Shanghai Chengjie Chemical Co. Ltd.

2.2. Synthesis of the photocatalysts

NH_2-MIL-125(Ti) was prepared by employing a facile one-pot process and then activated by solvents (Supporting information). Preparation of NH_2-MIL-125(Ti)/BiOCl composite was described below (Scheme 1): firstly, a given mass of NH_2-MIL-125(Ti) and 0.48 g Bi$(NO_3)_3{\cdot}5H_2O$ were added into 10 mL of 0.1 M mannitol solution and marked as solution A. 0.34 g [C_{16}mim]Cl was added into 10 mL of 0.1 M mannitol solution and marked as solution B. Solution B was mixed with solution A by drops with vigorous stirring and then stirred for 1 h. Then the suspension was transferred into 25 mL Teflon-lined autoclave and heated at 140 °C for 24 h in oven. The precipitate was washed several times with hot distilled water and alcohol. The composite was obtained after drying at 60 °C for 24 h. The as-prepared NH_2-MIL-125(Ti)/BiOCl materials with 5 wt%, 10 wt% and 15 wt% loading amount of NH_2-MIL-125(Ti) were marked as NM/BOC-5, NM/BOC-10 and NM/BOC-15, respectively. As a comparison, pure BiOCl was also prepared at the same condition without the introduction of NH_2-MIL-125(Ti).

2.3. Characterization

The crystalline structure of the materials was analyzed by X-ray diffraction (XRD, Rigaku D/Max-2500, Japan). This process employed Cu Kα radiation (λ = 1.54056 Å), a working current of 40 mA, a voltage of 40 kV, a scan speed of 5° min^{-1}, and a scan range of 5–80°. The morphology of the samples were observed via a transmission electron microscopy (TEM, Tecnai G2 F30 S-Twin, FEI, USA) equipped with an energy-dispersive X-ray spectrometry (EDS). X-ray photoelectron spectroscopy (XPS) was employed to determine its chemical composition. A UV-3600 UV–vis diffuse reflectance spectrometer (Shimadzu, Japan) was utilized to determine the absorption properties of light for the samples. $BaSO_4$ powder was used as the substrate material, and the wavelength coverage was from 200 to 800 nm. The fluorescence spectra was analyzed through fluorescence spectrometry (QuantaMaster 40, Horiba, Japan). N_2 adsorption-desorption instrument (TristarII 3020, USA) was used to measure the specific surface area and the pore structure of the samples. Thermal gravimetric analysis curves (TGA) were recorded on a thermal analyzer (TGA7, Perkin Elmer, USA) with a heating rate of 10 °C min^{-1} under nitrogen atmosphere. Raman spectra was measured by a Raman spectrometer (LabRAM HR Evolution, Horiba Instrument Inc., USA).

2.4. Evaluation of photocatalytic activity

The degradation of organic contaminants was conducted in a photocatalytic reactor with a reaction temperature of 30 ± 2 °C; TC and BPA acted as model pollutants. A 250 W Xe lamp with 400 nm cutoff filter simulated the solar light. During the photocatalytic tests, 0.05 g of samples were dispersed into aqueous solutions of TC (100 mL, 20 mg L^{-1}) and BPA (100 mL, 10 mg L^{-1}). The suspensions were stirred for 1 h in the darkness to achieve the adsorption-desorption equilibrium between the organic pollutants and catalysts. When the light source was turned on, 4 mL of the reaction solution was sampled at set intervals. The nanoparticles were removed from the resulting solution via the high-speed centrifugation. The concentration of TC was measured by monitoring its characteristic absorption at around 357 nm. BPA was quantified with a high-performance liquid chromatography system (Shimadzu Corp, Kyoto, Japan), which consists of an Aglient TC-C (18) column, an ultraviolet detector at 230 nm, and two Varian Prostar 210 pumps. The mobile phase was composed of methanol/water = 75:25

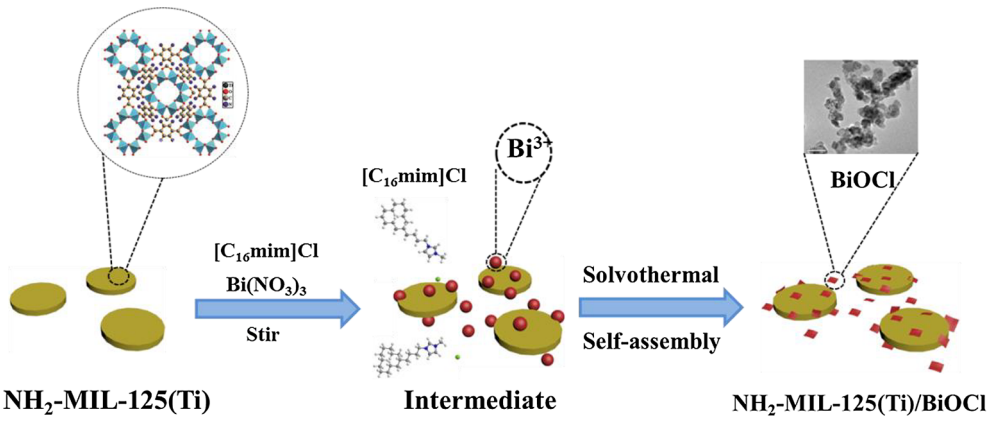

Scheme 1. Schematic illustration of the formation process for NH_2-MIL-125(Ti)/BiOCl composite.

(v/v). And the flow rate was 1 mL min^{-1}. 20 μL of the pollutant solution was injected.

2.5. Radical-trapping experiments

Reactive species trapping experiments were conducted to explore the main active species in the photocatalytic process. Nitrogen (N_2), ammonium oxalate (AO), tert-butanol (t-BuOH) and isopropyl alcohol (IPA) were employed as superoxide radicals ($O_2^{\cdot -}$), holes (h^+) and hydroxyl radicals ($^{\cdot}OH$) scavengers, respectively. During the photocatalytic tests, 0.05 g of the materials and 1 mM scavengers were added into 100 mL, 20 mg L^{-1} TC solution. After being stirred for 1 h in the darkness to ensure sufficient adsorption/desorption equilibrium, the suspensions were collected by centrifugation at every 30 min intervals after visible-light irradiation. The ESR spectrometer was conducted to further trap radicals by spin-trap reagent 5,5-dimethyl-1-pyrroline-N-oxide (DMPO) in water and methanol solution on a JES-FA 200 spectrometer (Bruker, Germany).

2.6. Photoelectrochemical measurements

An electrochemical work station (CHI 660B) was used to explore the photoelectrochemical properties of the materials. 5 mg samples were added into 1 mL of ethylene glycol and ultrasonicated for 1 h, 20 μL of the mixture solution was dropped on the ITO glass (0.5 cm × 1 cm, the conductive side) and dried at 100 °C for 12 h. A standard three electrode system was employed to record the photocurrents and electrochemical impedance spectra (EIS), which consists of working electrode (an ITO slice), counter electrode (a Pt wire) and reference electrode (a saturated Ag/AgCl).

3. Results and discussion

The crystal structure of the as-prepared materials was determined by XRD (Fig. 1). The obtained BiOCl displays a tetragonal phase (JCPDS card No. 06-0249) with well indexed (0 0 1), (1 0 1), (1 1 0), (1 0 2), (0 0 3), (1 1 2), (2 0 0), (2 0 1), (1 1 3), (2 1 1), (2 1 2), (1 1 4), (2 2 0), (2 1 4), (3 0 2) crystal planes [34]. The intense and sharp diffraction peaks demonstrate the highly crystalline. The XRD spectrum of NH_2-MIL-125(Ti) are consistent with the literature [35], which confirms the successful preparation of NH_2-MIL-125(Ti). After the incorporation of NH_2-MIL-125(Ti), all the diffraction peaks of the composite are nearly identical to those of pure BiOCl. No characteristic peaks of MOF can be detected, which may be ascribed to the high dispersion and low amount of MOF in the composite. Similar phenomenon can be observed in other systems [35,36].

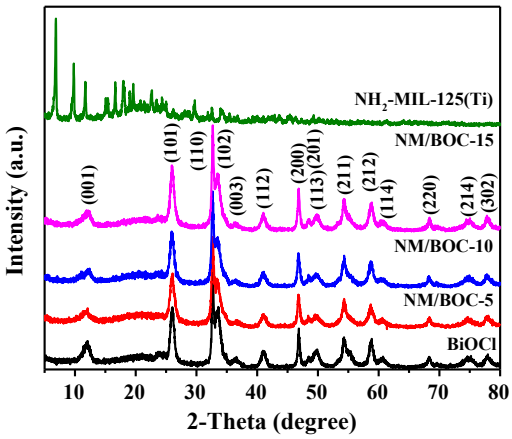

Fig. 1. XRD patterns of the as-prepared NH_2-MIL-125(Ti), BiOCl and NH_2-MIL-125(Ti)/BiOCl samples.

The chemical state and surface composition of the composite was investigated by XPS measurements. Fig. 2a displays a typical scan of NH_2-MIL-125(Ti)/BiOCl sample, which demonstrates that the Bi, Ti, C, O, Cl and N elements coexist in the composite. Fig. 2b displays the high-resolution XPS spectrum of Bi 4f. The peaks with binding energies at around 159.4 and 164.6 eV can be ascribed to Bi 4f7/2 and Bi 4f5/2 of Bi^{3+} in BiOCl [37]. The O 1s peak centered at 530.2 eV is assigned to the oxygen in BiOCl (Fig. 2c). In Fig. 2d, the double peaks located at 198.2 and 199.8 eV can be owing to the Cl 2p3/2 and Cl 2p1/2 of chloride ion [37]. The high-resolution XPS spectrum of C 1s (Fig. 2e) can be split into four distinct peaks, attributed to C═O (288.8 eV), C—C (286.6 eV), C—N (285.3 eV) and C═C (284.6 eV) of NH_2-MIL-125(Ti) [38]. The high-resolution spectra of Ti 2p further proves the existence of NH_2-MIL-125(Ti) in the composite (Fig. 2f). The two well-defined peaks at the binding energies of 465.0 eV and 459.2 eV can be attributed to Ti 2p1/2 and Ti 2p3/2, which show that titanium bonded to oxygen remain in oxidation state IV [38]. Notably, the peak of Ti 2p1/2 displays a broad bump, which can be explained by the overlap between Bi 4d3/2 at 466.6 eV and Ti 2p1/2 at 465.0 eV [35,39]. The high-resolution XPS spectrum (Fig. 2g) of N 1 s indicates the existence of N element. These pieces of evidence confirm the co-existence of BiOCl and MOF in the composite.

Infrared and Raman analysis were conducted to further demonstrate the interaction between MOF and BiOCl in the composite. In Fig. 3a, a sharp peak at around 525 cm^{-1} is attributed to the Bi-O stretching mode [9]. The absorption band appears at 1463 cm^{-1} is designated to the stretching vibration of carboxylate group of NH_2-MIL-125(Ti) (Fig. S1) and NH_2-MIL-125(Ti)/BiOCl composite [35]. The Raman spectra of BiOCl and NM/BOC-10 are shown in Fig. 3b. For BiOCl, the Raman peaks at around 60.6 cm^{-1} and 142.4 cm^{-1} belong to internal A_{1g} and external A_{1g} of Bi—Cl stretching vibration. The band at 199.2 cm^{-1} can be ascribed to E_g inherent Bi—Cl stretching mode [40]. After the incorporation of MOF, the bands at 142.4 cm^{-1} and 199.2 cm^{-1} show a slight blue-shift compared to BiOCl. This demonstrates that NH_2-MIL-125(Ti) is coordinated with BiOCl host via chemical bonds, not just a simple mixture of two samples [34]. These results are in concordance with the XPS data.

To explore the content of MOF in the composite, thermogravimetric analysis was conducted from 30 °C to 800 °C under nitrogen atmosphere. As depicted in Fig. S2, BiOCl displays a rapid decomposition between 500 °C and 700 °C. As for NM/BOC-10, the weight loss between 500 °C and 700 °C significantly increases. This is not only because of the loss of BiOCl, but also result from the themolysis of NH_2-MIL-125(Ti). Collapse of the framework of NH_2-MIL-125(Ti) between 500 °C and 600 °C, as a result of the decomposition of NH_2-MIL-125(Ti) into thermostable TiO_2 [35]. Through the TGA curves, the content of MOF in NM/BOC-10 is found to be about 10 wt%.

The samples' morphology was examined by SEM and TEM. In Fig. S5, the size of the obtained BiOCl nanosheets is less than 100 nm. In Fig. S3, NH_2-MIL-125(Ti) sample displays an inerratic bulk structure shape with the size range at 100–500 nm. It can be observed that BiOCl nanosheets aggregate on outer surface of MOF. The TEM images of NM/BOC-10 show that BiOCl nanosheets are well attached on the surface of MOF (Fig. 4a and b). The HRTEM image of NM/BOC-10 shown in Fig. 4c presents clearly lattice fringes with spacing of 0.344 nm and 0.275 nm, corresponding to the tetragonal phase BiOCl (0 0 1) and (1 1 0) planes [9,37]. The EDX spectrum (Fig. 4d) and EDX element mapping of NM/BOC-10 (Fig. S4) demonstrate the presence of Bi, C, N, O, Cl and Ti elements in the composite. Based on these characterizations, it can be concluded that the heterojunction structure is formed, which is supposed to improve the separation and transfer efficiency of photoinduced charge carriers.

The porous structure and specific surface area of the prepared materials were studied by nitrogen adsorption-desorption analysis, and the results were displayed in Fig. 5 and Fig. S6. The BET specific surface area of bare NH_2-MIL-125(Ti) is found to be 769.70 $m^2 g^{-1}$, which

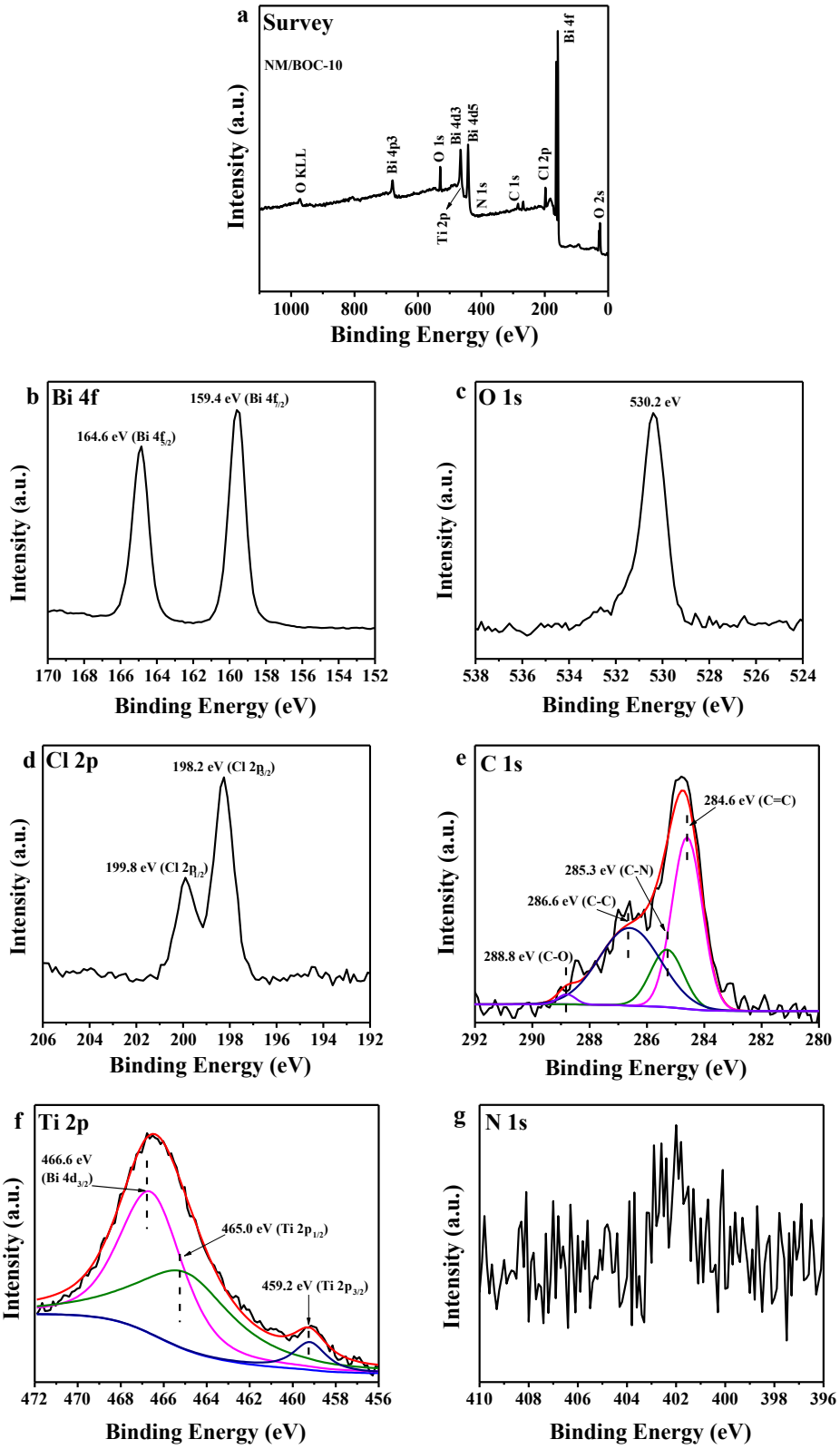

Fig. 2. XPS spectra of NM/BOC-10 sample (a) Survey of the sample, (b) Bi 4f, (c) O 1s, (d) Cl 2p, (e) C 1s, (f) Ti 2p, (g) N 1s.

agrees with the previous reports [35,38]. For pure BiOCl, the corresponding value is 29.41 $m^2 g^{-1}$. The specific surface area of the composite grows significantly with the increasing amount of MOF. The surface adsorption of organic contaminants on the photocatalyst acts as a key factor in photocatalytic performance [41]. Hence, the adsorption experiment was carried out to verify this finding. In Fig. S7, the adsorption of TC reached equilibrium at around 60 min. As the amount of MOF rises, the adsorption capacity of TC improves, which is in consistent with the BET specific surface area.

The photocatalytic activities of the obtained composite were first evaluated via the photocatalytic degradation of TC under visible light irradiation. Single BiOCl and NH_2-MIL-125(Ti) were also employed for

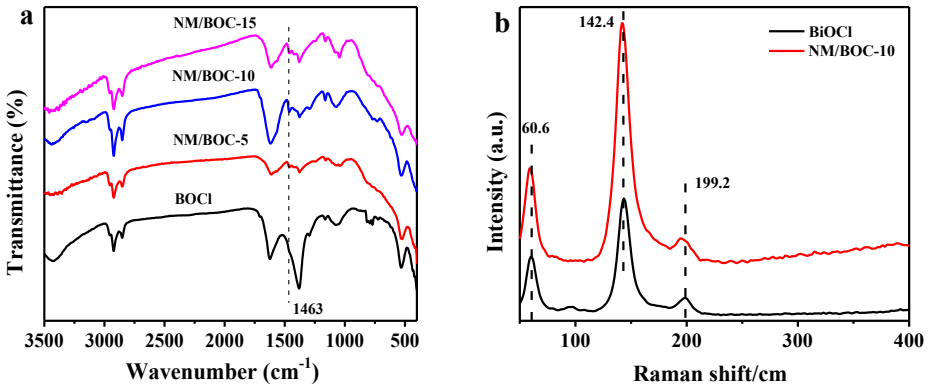

Fig. 3. (a) FT-IR spectra of BiOCl and NH_2-MIL-125(Ti)/BiOCl samples, and (b) Raman spectra of BiOCl and NM/BOC-10.

comparison. As shown in Fig. 6a, self-photodegradation of TC is ignored without any photocatalyst. Only about 5% degradation occurs with single NH_2-MIL-125(Ti), while nearly 40% degradation occurs in the presence of BiOCl during 2 h of visible light irradiation. It is suggested that oxygen vacancy could slightly broaden the absorption region in others' study [42]. To verify this assumption, the low-temperature electron paramagnetic resonance (EPR) spectroscopy was carried out. As shown in Fig. S8, BiOCl sample turns out to possess a typical signal centered at g = 2.001, due to the electrons trapped on the oxygen vacancies [43]. After the incorporation of MOF, NM/BOC-10 presents a much higher degradation efficiency (~78%) than that of single BiOCl or MOF via a pseudo first-order kinetic reaction (Fig. 6b and c). It is probably attributed to that MOF contributes to the separation of photoinduced charge carriers, which enhance the degradation efficiency of TC by the interface contact between BiOCl and MOF [44]. Obviously, NM/BOC-10 displays the highest degradation efficiency at a rate constant of 0.0141 min^{-1}, which is about 3.5 times and 35 times as that of BiOCl (0.004 min^{-1}) and MOF (0.0004 min^{-1}). Hence, NM/BOC-10 serves as the optimal photocatalyst in the follow-up experiments. Nevertheless, as the loading amount of MOF increases to 15%, the

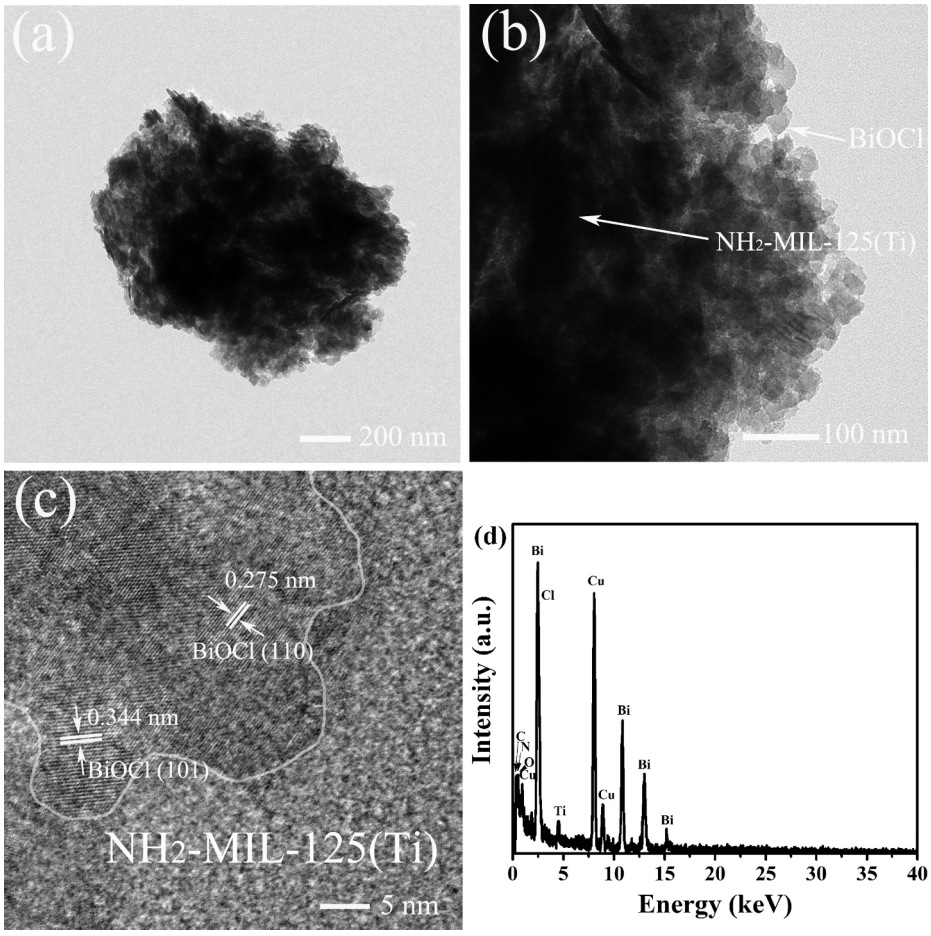

Fig. 4. TEM images of (a) (b) NM/BOC-10, (c) HRTEM image of NM/BOC-10, and (d) EDX spectrum of NM/BOC-10.

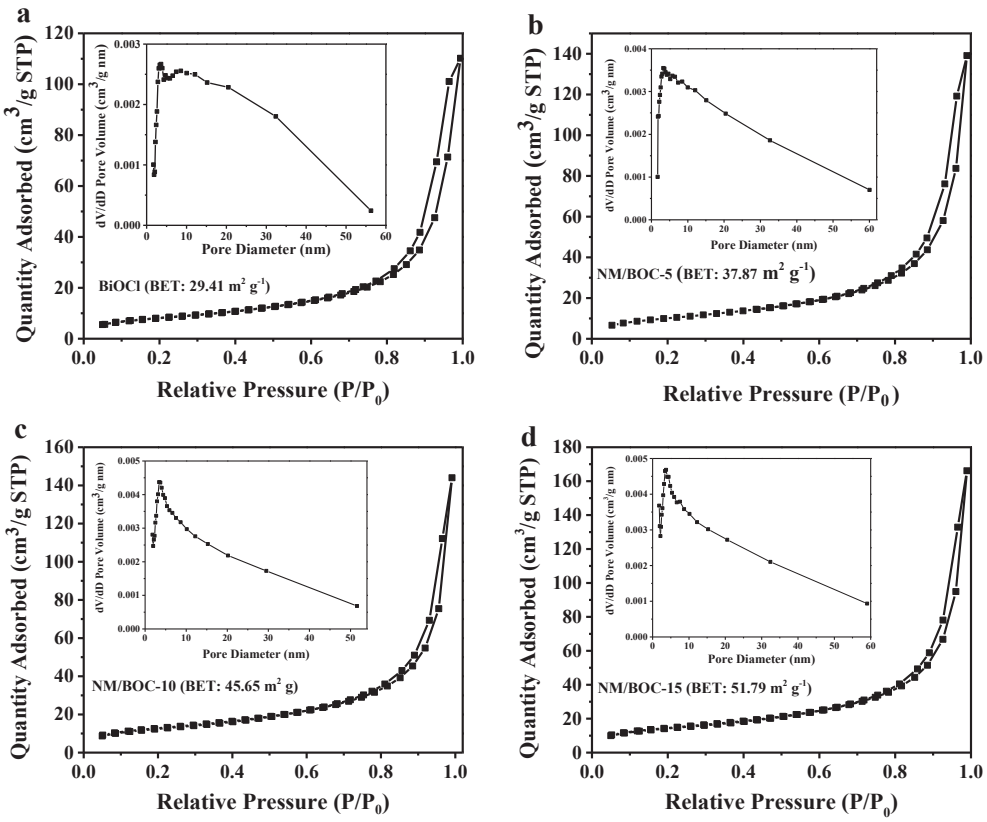

Fig. 5. Nitrogen adsorption-desorption isotherms of BiOCl and NH_2-MIL-125(Ti)/BiOCl composite with different weight ratio of NH_2-MIL-125(Ti).

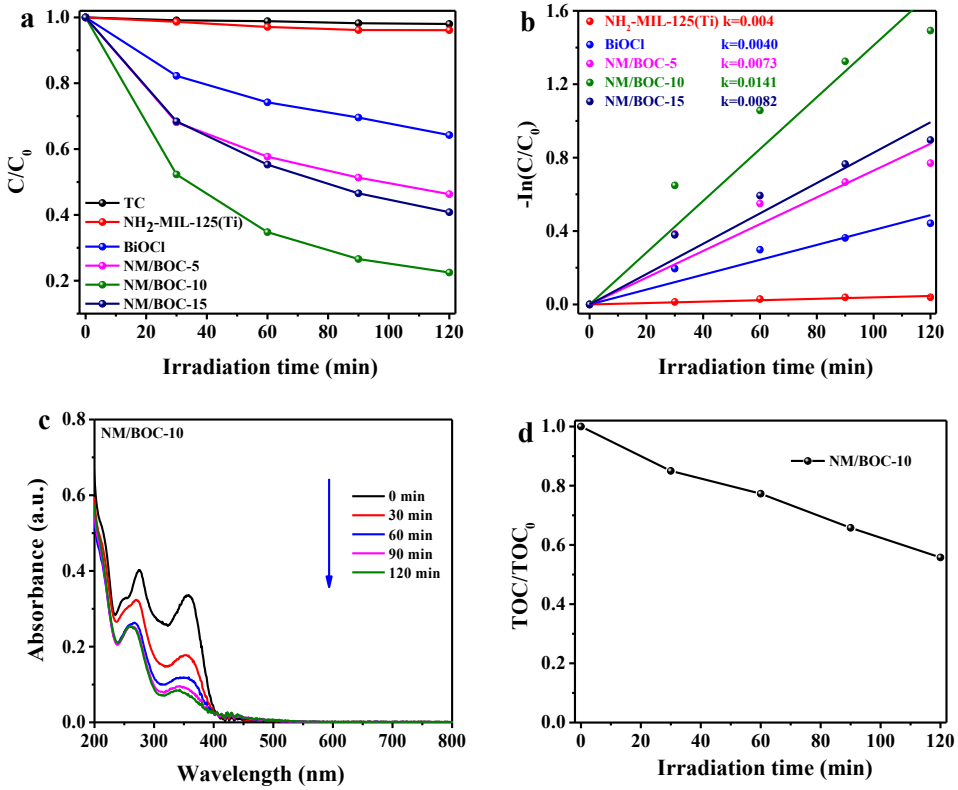

Fig. 6. (a) Dynamic curves of TC photodegradation under visible light irradiation, (b) plots of -In(C/C_0) versus irradiation time and reaction rate constant k obtained from linear fitting, (c) absorption spectra changes of TC over NM/BOC-10, (d) the decrease of TOC during the photodegradation of TC on NM/BOC-10.

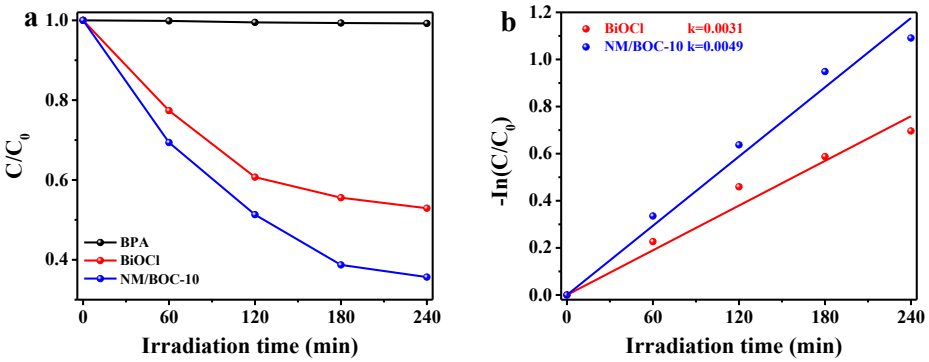

Fig. 7. (a) Photocatalytic degradation of BPA in the presence of BiOCl and NM/BOC-10 under visible light irradiation, (b) plots of -In(C/C_0) versus irradiation time and reaction rate constant k obtained from linear fitting.

photocatalytic efficiency of NM/BOC-15 declines, despite the improvement in adsorption capacity of NM/BOC-15 (Fig. S7). One possible reason could be that the improved amount of MOF overlay the active sites of BiOCl, which in turn reduce the degradation efficiency [45]. Total organic carbon (TOC) experiment was also conducted to investigate the degradation of TC by NM/BOC-10 (Fig. 6d). Under irradiation for 2 h, almost 45.2% of TC is mineralized. It implies that TC can be degraded by the composite photocatalyst under visible light irradiation.

Bisphenol A (BPA), a raw material in chemical engineering, has been extensively produced and used. Nevertheless, studies revealed that the surplus of BPA in the environment may cause endocrine disorders and pose threat to the health of children and fetus [46]. Therefore, the removal of BPA has become a popular area of research. Fig. 7a displays the degradation curves of BPA over BiOCl and NM/BOC-10. After 4 h, nearly 65% of BPA was removed over NM/BOC-10, while the degradation efficiency of pure BiOCl was only 48%. As a result, NM/BOC-10 possesses better photocatalytic activity (Fig. 7b). The results above indicate that the incorporation of NH_2-MIL-125(Ti) acts as an important role in enhancing photocatalytic performance under visible light.

It is well established that the stability of the photocatalyst is extremely important during the photodegradation reaction process. As depicted in Fig. S9, the photodegradation rate of TC does not decline greatly after five cycles under visible light irradiation, indicating that the as-prepared material is stable, and promising in large-scale application. Moreover, the XRD pattern of the used sample after the cycling experiment was conducted to confirm the stability of the photocatalyst. In Fig. S10, no obvious discrepancy is observed. The composite exhibits high stability and does not change in the crystal structure.

The optical properties of the as-prepared samples were analyzed by UV–vis diffuse reflectance spectra (DRS), and the data was presented in Fig. 8a. Pure BiOCl displays a typical DRS as reported in other literatures [34,37], with an absorption edge around 380 nm, corresponding to the optical bandgap of 3.31 eV (Fig. S11). Meanwhile, NH_2-MIL-125(Ti) possesses a bandgap of approximately 2.60 eV with the absorption edge of 520 nm. After the incorporation of MOF, it is interesting to find that the composite demonstrates more intense absorption in visible light. The enhanced optical absorption allows NH_2-MIL-125(Ti)/BiOCl composite to harvest more visible light and generate more reactive species involved in the photocatalytic reaction [47]. It is impressive that the photocatalytic performance of BiOCl is remarkably improved after the combination of MOF.

As is known to all, photoluminescence (PL) is widely employed to investigate the separation and transfer efficiency of photoexcited electron-hole pairs, since the charge recombination leads to the enhancement of PL emission signal. In Fig. 8b, as compared with pure BiOCl, NM/BOC-10 displays lower emission peak at around 360 nm. It implies that the high charge recombination is effectively inhibited after the incorporation of MOF. But the lower PL emission peak of NH_2-MIL-125(Ti) is not in consistent with the photocatalytic performance. The results indicate that PL is not the only way to prove the photocatalytic activity [35].

Electrochemical performance is another measurement for evaluating the separation and transfer efficiency of photoinduced charge carriers in the photocatalytic system. The transient photocurrent responses of the materials were recorded under visible light irradiation and the results were shown in Fig. 8c. The photocurrent responses of the materials remain reproducible after four intermittent on-off irradiation cycles. And NM/BOC-10 displays the highest photocurrent density, demonstrating lower recombination and longer lifetime of photoexcited electron-hole pairs than pure BiOCl or NH_2-MIL-125(Ti). It also shows that the separation efficiency of photogenerated carriers can be enhanced with the introducing of MOF [35]. Moreover, EIS was performed to further explore the charge transfer properties of the as-prepared samples. As depicted in Fig. 8d, NM/BOC-10 shows the smallest arc radius in comparison with other materials. It has much lower electron-transfer resistance than BiOCl or NH_2-MIL-125(Ti), resulting in higher charge separation efficiency [44]. It is evident that the incorporation of NH_2-MIL-125(Ti) is able to improve the absorption capacity of visible light, charge separation efficiency and eventually the photocatalytic performance.

With the goal to achieve a better understanding of the photocatalytic mechanism of NH_2-MIL-125(Ti)/BiOCl composite, the radical-trapping experiments were conducted by adding individual scavengers in the degradation experiments. Isopropanol (IPA) and tert-butanol were used for quenching hydroxyl radicals ($^{\cdot}OH$), nitrogen (N_2) for superoxide radicals ($O_2^{\cdot -}$), and ammonium oxalate (AO) for holes, respectively [37,41]. As shown in Fig. 9, the photocatalytic performance is inhibited significantly after the introduction of N_2 or AO, while the addition of IPA or tert-butanol exerts little influence on the photocatalytic activity. It is assumed that $O_2^{\cdot -}$ and holes act as the major active species in the photocatalytic reaction, whereas $^{\cdot}OH$ does not behave as the main reactive species. Therefore, the promoted generation of holes and $O_2^{\cdot -}$ could ultimately enhance the photocatalytic performance.

In order to verify the generation of $O_2^{\cdot -}$ in the photocatalytic system, the ESR spin-trap technique was introduced in this study. In Fig. 10a, the intensity of the DMPO-$O_2^{\cdot -}$ adducts can be neglected in the dark, but it becomes stronger after the irradiation of visible light, showing that $O_2^{\cdot -}$ acts as an important role during the photocatalytic reaction. Additionally, the $O_2^{\cdot -}$ signal intensity of NM/BOC-10 is obviously stronger than that of BiOCl alone. It implies that the amount of $O_2^{\cdot -}$ radicals generated on the surface of NM/BOC-10 is higher than that of BiOCl under the irradiation of visible light. Nevertheless, the characteristic peaks of DMPO-$^{\cdot}OH$ adducts for both BiOCl and NM/BOC-10 cannot be observed under visible light irradiation (Fig. 10b).

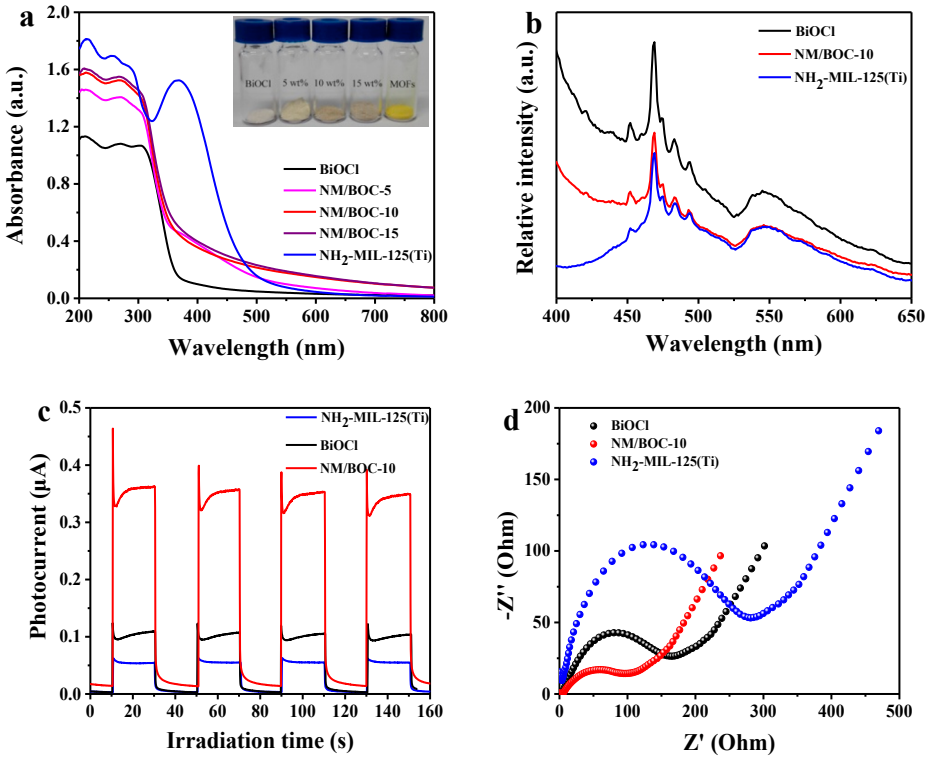

Fig. 8. (a) UV–vis diffuse reflectance spectra of the obtained materials, (b) PL spectra, (c) transient photocurrent responses and (d) EIS Nyquist of NH_2-MIL-125(Ti), BiOCl and NM/BOC-10.

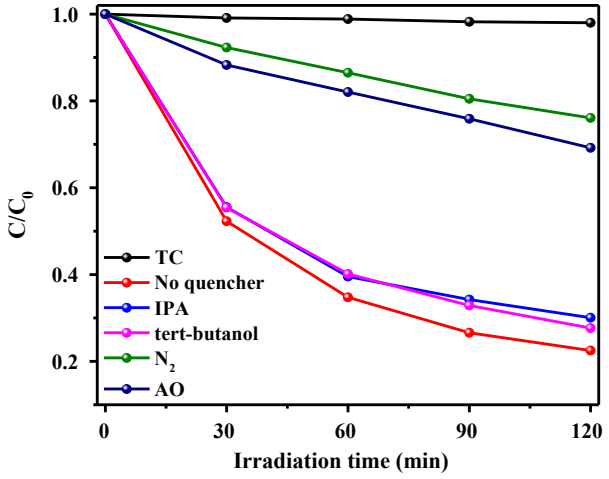

Fig. 9. Comparsion of the photocatalytic performance of NM/BOC-10 for the degradation of TC with or without adding IPA, tert-butanol, N_2 and AO under visible light irradiation.

The ESR results validate that holes and $O_2^{\cdot -}$ participate in the photocatalytic reaction, which is in accord with the radical-trapping experiments.

It is well known that the band alignment is critical for heterostructure photocatalyst with high photocatalyst ability. The XPS valence band (VB) spectra was carried out to identify the band position of BiOCl and NH_2-MIL-125(Ti). In Fig. 11, the position of valence band is measured to be 1.35 eV for BiOCl material by XPS VB spectra. While the HOMO (Highest Occupied Molecular Orbital) of NH_2-MIL-125(Ti) is measured to be 2.15 eV. Based on the bandgap value acquired by DRS analysis (Fig. S11), the conduction band (CB) energy levels of the two samples can be estimated by $E_{CB} = E_{VB} - E_g$. The conduction band of BiOCl is approximately −1.96 eV, while the LUMO (Lowest Occupied Molecular Orbital) of NH_2-MIL-125(Ti) is calculated to be −0.62 eV.

Combining all the results shown above, a plausible photocatalytic mechanism for the composite is presented (Fig. 12). When the visible light irradiates, the electrons in the VB of BiOCl can be excited and transferred to the CB, leaving the holes in the VB. However, the photoexcited electrons quickly recombine with the holes, which is not preferred in the photocatalytic system. After the incorporation of NH_2-MIL-125(Ti), the LUMO of NH_2-MIL-125(Ti) is about −0.45 eV, which is much higher than that of BiOCl (−1.96 eV). Hence, the photoexcited electrons could transfer from the CB of BiOCl to the LUMO of NH_2-MIL-125(Ti). In contrast, the HOMO of NH_2-MIL-125(Ti) (+2.02 eV) is much higher than that of BiOCl (+1.35 eV). As a result, the photogenerated holes could migrate from the HOMO of NH_2-MIL-125(Ti) to that of BiOCl. Therefore, the photoinduced charge carriers can be transferred efficiently in the photocatalytic system, leading to a significantly enhanced photocatalytic performance.

4. Conclusions

In summary, we prepared NH_2-MIL-125(Ti)/BiOCl composite photocatalyst through a simple hydrothermal process. The enhanced visible-light photocatalytic activity of BiOCl was achieved by incorporating NH_2-MIL-125(Ti). Meanwhile, matching energy level structures could accelerate the separation efficiency of photoinduced charge carriers. In addition, the large internal surface area of NH_2-MIL-125(Ti) enables the composite to adsorb more contaminants and reactive species, promoting the photocatalytic activity. Consequently, the composite displayed improved photocatalytic performance on TC and BPA degradation. Both $O_2^{\cdot -}$ and holes were determined to be the main reactive species via radical-trapping experiments, XPS, VB spectra and ESR analysis. Last but by no mean the least, the favorable durability and stability of NH_2-MIL-125(Ti)/BiOCl composite makes it a promising photocatalyst in environmental purification.

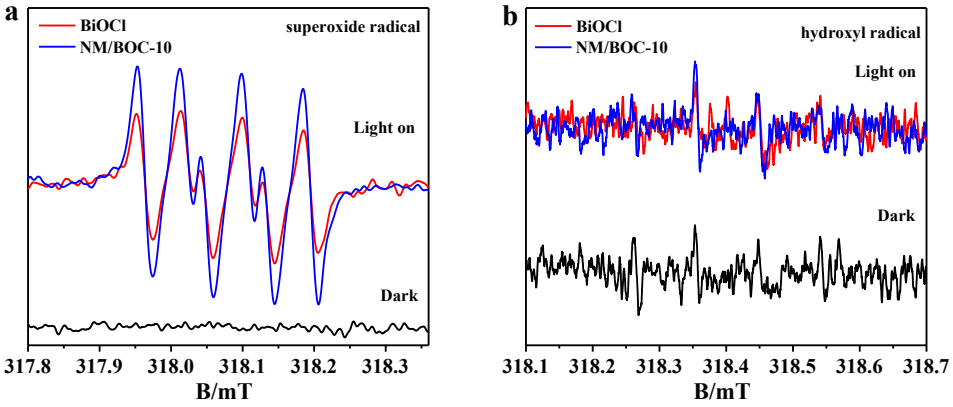

Fig. 10. DMPO spin-trapping ESR spectra recorded with BiOCl and NM/BOC-10 in (a) methanol dispersion (for DMPO-$O_2^{\cdot -}$) and (b) aqueous dispersion (for DMPO-$^{\cdot}$OH) under visible light irradiation.

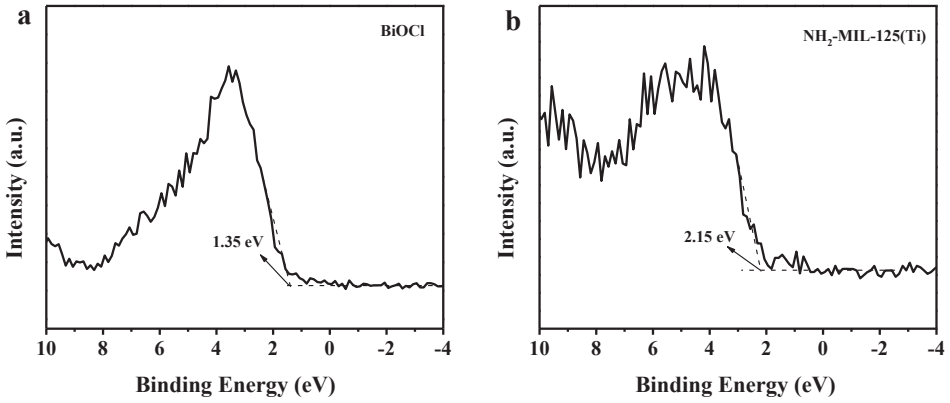

Fig. 11. Valence-band XPS spectra of (a) BiOCl and (b) NH_2-MIL-125 (Ti).

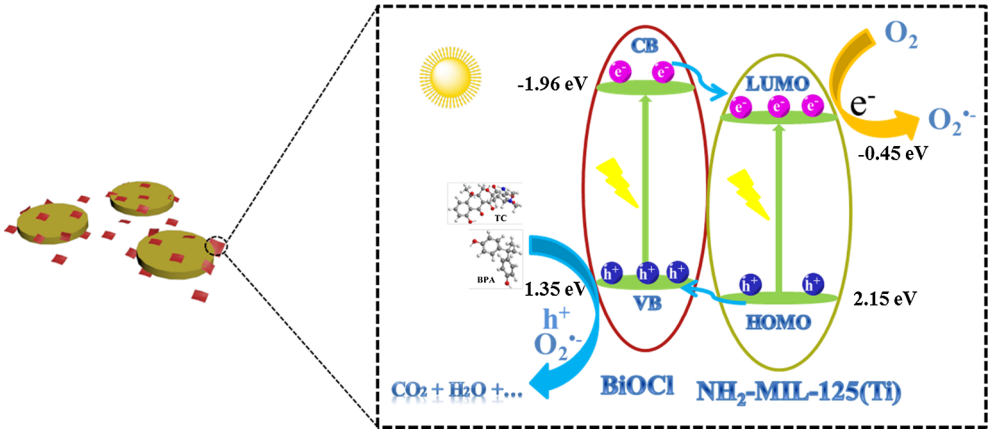

Fig. 12. Proposed charge transfer mechanism of NH_2-MIL-125(Ti)/BiOCl composite.

Acknowledgements

This work was financially supported by the National Natural Science Foundation of China (Nos. 21476098, 21471069 and 21576123), and Jiangsu University Scientific Research Funding (No. 11JDG0146).

Appendix A. Supplementary material

Supplementary data to this article can be found online at https://doi.org/10.1016/j.apsusc.2018.10.020.

References

[1] A. Shah, S. Shahzad, A. Munir, M.N. Nadagouda, G.S. Khan, D.F. Shams, D.D. Dionysiou, U.A. Rana, Micelles as soil and water decontamination agents, Chem. Rev. 116 (2016) 6042–6074.
[2] Y. Wu, H. Wang, W.G. Tu, S.Y. Wu, Y. Liu, Y.Z. Tan, H.J. Luo, X.Z. Yuan, J.W. Chew, Petal-like CdS nanostructures coated with exfoliated sulfur-doped carbon nitride via chemically activated chain termination for enhanced visible-light-driven photocatalytic water purification and H_2 generation, Appl. Catal. B 229 (2018) 181–191.
[3] Y. Wu, H. Wang, W.G. Tu, Y. Liu, S.Y. Wu, Y.Z. Tan, J.W. Chew, Construction of hierarchical 2D–2D $Zn_3In_2S_6$/fluorinated polymeric carbon nitride nanosheets photocatalyst for boosting photocatalytic degradation and hydrogen production performance, Appl. Catal. B 233 (2018) 58–69.

[4] Y. Wu, H. Wang, Y.M. Sun, T. Xiao, W.G. Tu, X.Z. Yuan, G.M. Zeng, S.Z. Li, J.W. Chew, Photogenerated charge transfer via interfacial internal electric field for significantly improved photocatalysis in direct Z-scheme oxygen-doped carbon nitrogen/CoAl-layered double hydroxide heterojunction, Appl. Catal. B 227 (2018) 530–540.

[5] G. Liu, L.C. Yin, P. Niu, W. Jiao, H.M. Cheng, Visible-light-responsive b-rhombohedral boron photocatalysts, Angew. Chem. Int. Ed. 52 (2013) 6242–6245.

[6] H. Wang, Y. Wu, M.B. Feng, W.G. Tu, T. Xiao, T. Xiong, H.X. Ang, X.Z. Yuan, J.W. Chew, Visible-light-driven removal of tetracycline antibiotics and reclamation of hydrogen energy from natural water matrices and wastewater by polymeric carbon nitride foam, Water Res. 114 (2018) 215–225.

[7] M. Dahl, Y.D. Liu, Y.D. Yin, Composite titanium dioxide nanomaterials, Chem. Rev. 114 (2014) 9853–9889.

[8] S. Linic, P. Christopher, D.B. Ingram, Plasmonic-metal nanostructures for efficient conversion of solar to chemical energy, Nat. Mater. 10 (2011) 911–921.

[9] J.X. Xia, J. Di, H.T. Li, H. Xu, H.M. Li, S.J. Guo, Ionic liquid-induced strategy for carbon quantum dots/BiOX (X = Br, Cl) hybrid nanosheets with superior visible light-driven photocatalysis, Appl. Catal. B 181 (2016) 260–269.

[10] J. Li, H. Li, G.M. Zhan, L.Z. Zhang, Solar water splitting and nitrogen fixation with layered bismuth oxyhalides, Acc. Chem. Res. 50 (2017) 112–121.

[11] J. Li, Y. Yu, L.Z. Zhang, Bismuth oxyhalide nanomaterials: layered structures meet photocatalysis, Nanoscale 6 (2014) 8473–8488.

[12] A.M. Ganose, M. Cuff, K.T. Butler, A. Walsh, D.O. Scanlon, Interplay of orbital and relativistic effects in bismuth oxyhalides: BiOF, BiOCl, BiOBr, and BiOI, Chem. Mater. 28 (2016) 1980–1984.

[13] J. Di, J.X. Xia, H.M. Li, S.J. Guo, S. Dai, Bismuth oxyhalide layered materials for energy and environmental applications, Nano Energy 41 (2017) 172–192.

[14] J. Di, C. Chen, S.Z. Yang, M.X. Ji, C. Yan, K.Z. Gu, J.X. Xia, H.M. Li, S.Z. Li, Z. Liu, Defect engineering in atomically-thin bismuth oxychloride towards photocatalytic oxygen evolution, J. Mater. Chem. A 5 (2017) 14144–14151.

[15] H. Wang, X.Z. Yuan, Y. Wu, G.M. Zeng, W.G. Tu, C. Sheng, Y.C. Deng, F. Chen, J.W. Chew, Plasmonic Bi nanoparticles and BiOCl sheets as cocatalyst deposited on perovskite-type $ZnSn(OH)_6$ microparticle with facet-oriented polyhedron for improved visible-light-driven photocatalysis, Appl. Catal. B 209 (2017) 543–553.

[16] X.J. Wang, Q. Wang, F.T. Li, W.Y. Yang, Y. Zhao, Y.J. Hao, S.J. Liu, Novel BiOCl-C_3N_4 heterojunction photocatalysts: in situ preparation via an ionic-liquid-assisted solvent-thermal route and their visible-light photocatalytic activities, Chem. Eng. J. 234 (2013) 361–371.

[17] Q.Y. Li, Z.P. Guan, D. Wu, X.G. Zhao, S.Y. Bao, B.Z. Tian, J.L. Zhang, Z-Scheme BiOCl-Au-CdS heterostructure with enhanced sunlight-driven photocatalytic activity in degrading water dyes and antibiotics, ACS Sustain. Chem. Eng. 5 (2017) 6958–6968.

[18] Y. Mi, L. Wen, Z. Wang, D. Cao, Y. Fang, Y. Lei, Building of anti-restack 3D BiOCl hierarchitecture by ultrathin nanosheets towards enhanced photocatalytic activity, Appl. Catal. B 176–177 (2015) 331–337.

[19] Y. Wu, B. Yuan, M. Li, W.H. Zhang, Y. Liu, C. Li, Well-defined BiOCl colloidal ultrathin nanosheets: synthesis, characterization, and application in photocatalytic aerobic oxidation of secondary amines, Chem. Sci. 6 (2015) 1873–1878.

[20] K. Zhang, D. Zhang, J. Liu, K. Ren, H. Luo, Y. Peng, G. Li, X. Yu, A novel nanoreactor framework of iodine-incorporated BiOCl core-shell structure: enhanced light-harvesting system for photocatalysis, CrystEngComm 14 (2012) 700–707.

[21] L. Zhang, W.Z. Wang, S.M. Sun, Y.Y. Sun, E.P. Gao, J. Xu, Water splitting from dye wastewater: a case study of BiOCl/copper(II) phthalocyanine composite photocatalyst, Appl. Catal. B. 132–133 (2013) 315–320.

[22] Y. Yu, C. Cao, H. Liu, P. Li, F. Wei, Y. Jiang, W. Song, A Bi/BiOCl heterojunction photocatalyst with enhanced electron-hole separation and excellent visible light photodegrading activity, J. Mater. Chem. A 2 (2014) 1677–1681.

[23] C.H. Wang, X.L. Liu, N.K. Demir, J.P. Chen, K. Li, Applications of water stable metal-organic frameworks, Chem. Soc. Rev. 45 (2016) 5107–5134.

[24] J.L. Wang, C. Wang, W.B. Lin, Metal-organic frameworks for light harvesting and photocatalysis, ACS Catal. 2 (2012) 2630–2640.

[25] T.M. McDonald, J.A. Mason, X. Kong, E.D. Bloch, D. Gygi, A. Dani, V. Ceocella, F. Ciordanino, S.O. Odoh, W.S. Drisdell, B. Vlaisavljevich, A.L. Dzubak, R. Poloni, S.K. Schnell, N. Planas, K. Lee, T. Pascal, L.F. Wan, D. Prendergast, J.B. Neaton, B. Smit, J.B. Kortright, L. Gagliardi, S. Bordiga, J.A. Long, Cooperative insertion of CO_2 in diamine-appended metal-organic frameworks, Nature 519 (2015) 303–308.

[26] S.T. Meek, J.A. Greathouse, M.D. Allendorf, Metal-oragnic frameworks: a rapidly growing class of versatile nanoporous materials, Adv. Mater. 23 (2011) 249–267.

[27] S.B. Wang, X.C. Wang, Multifunctional metal-organic frameworks for photocatalysis, Small 11 (2015) 3097–3112.

[28] L.Z. Huang, B.S. Liu, Synthesis of a novel and stable reduced graphene oxide/MOF hybrid nanocomposite and photocatalytic performance for the degradation of dyes, RSC Adv. 6 (2016) 17873–17879.

[29] Y. Horiuchi, T. Toyao, M. Saito, K. Mochizuki, M. Iwata, H. Higashimura, M. Anpo, M. Matsuoka, Visible-light-promoted photocatalytic hydrogen production by using an amino-functionalized Ti(IV) metal-organic framework, J. Phys. Chem. C 116 (2012) 20848–20853.

[30] Y.H. Fu, D.R. Sun, Y.J. Chen, R.K. Huang, Z.X. Ding, X.Z. Fu, Z.H. Li, An amine-functionalized titanium metal-organic framework photocatalyst with visible-light-induced activity for CO_2 reduction, Angew. Chem. Int. Ed. 51 (2012) 3364–3367.

[31] Y.H. Fu, L. Sun, H. Yang, L. Xu, F.M. Zhang, W.D. Zhu, Visible-light-induced aerobic photocatalytic oxidation of aromatic alcohols to aldehydes over Ni-doped NH_2-MIL-125(Ti), Appl. Catal. B 187 (2016) 212–217.

[32] M.C. Wen, K. Mori, Y. Kuwahara, T.C. An, H. Yamashita, Design and architecture of metal organic frameworks for visible light enhanced hydrogen production, Appl. Catal. B 218 (2017) 555–569.

[33] Z.B. Wu, X.Z. Yuan, J. Zhang, H. Wang, L.B. Jiang, G.M. Zeng, Photocatalytic decontamination of wastewater containing organic dyes by metal-organic frameworks and their derivatives, ChemCatChem 9 (2017) 41–64.

[34] Y. Mi, L.Y. Wen, Z.J. Wang, D.W. Cao, R. Xu, Y.G. Fang, Y.L. Zhou, Y. Lei, Fe(III) modified BiOCl ultrathin nanosheet towards high-efficient visible-light photocatalyst, Nano Energy 30 (2016) 109–117.

[35] S.R. Zhu, P.F. Liu, M.K. Wu, W.N. Zhao, G.C. Li, K. Tao, F.Y. Yi, L. Han, Enhanced photocatalytic performance of BiOBr/NH_2-MIL-125(Ti) composite for dye degradation under visible light, Dalton Trans. 45 (2016) 17521–17529.

[36] J. Di, J.X. Xia, M.X. Ji, B. Wang, S. Yin, Q. Zhang, Z.G. Chen, H.M. Li, Advanced photocatalytic performance of graphene-like BN modified BiOBr flower-like materials for the removal of pollutants and mechanism insight, Appl. Catal. B 183 (2016) 254–262.

[37] J. Di, J.X. Xia, M.X. Ji, B. Wang, S. Yin, Q. Zhang, Z.G. Chen, H.M. Li, Carbon quantum dots modified BiOCl ultrathin nanosheets with enhanced molecular oxygen activation ability for broad spectrum photocatalytic properties and mechanism insight, ACS Appl. Mater. Interfaces 7 (2015) 20111–20123.

[38] H. Liu, J. Zhang, D. Ao, Construction of heterostructured $ZnIn_2S_4$@NH_2-MIL-125(Ti) nanocomposites for visible-light-driven H_2 production, Appl. Catal. B 221 (2018) 433–442.

[39] Y. Zhao, X. Huang, X. Tan, T. Yu, X.L. Li, L.B. Yang, S.C. Wang, Fabrication of BiOBr nanosheets@TiO_2 nanobelts p-n junction photocatalysts for enhanced visible-light activity, Appl. Surf. Sci. 365 (2016) 209–217.

[40] J.E.D. Davies, Solid state vibrational spectroscopy-III[1] The infrared and raman spectra of the bismuth (III) oxide halides, J. Inorg. Nucl. Chem. 35 (1973) 1531–1534.

[41] B. Wang, J. Di, P.F. Zhang, J.X. Xia, S. Dai, H.M. Li, Ionic liquid-induced strategy for porous perovskite-like $PbBiO_2Br$ photocatalysts with enhanced photocatalytic activity and mechanism insight, Appl. Catal. B 206 (2017) 127–135.

[42] C.Y. Wang, Y.J. Zhang, W.K. Wang, D.N. Pei, G.X. Huang, J.J. Chen, X. Zhang, H.Q. Yu, Enhanced photocatalytic degradation of bisphenol A by co-doped BiOCl nanosheets under visible light irradiation, Appl. Catal. B 221 (2018) 320–328.

[43] H. Wang, D.Y. Yong, S.C. Chen, S.L. Jiang, X.D. Zhang, W. Shao, Q. Zhang, W.S. Yan, B.C. Pan, Y. Xie, Oxygen-vacancy-mediated exciton dissociation in BiOBr for boosting charge-carrier-involved molecular oxygen activation, J. Am. Chem. Soc. 140 (2018) 1760–1766.

[44] Y.H. Liang, R. Shang, J.R. Lu, L. Liu, J.S. Hu, W.Q. Cui, Ag_3PO_4@UMOFNs core-shell structure: two-dimensional MOFs promoted photoinduced charge separation and photocatalysis, ACS Appl. Mater. Interfaces 10 (2018) 8758–8769.

[45] J.J. Wang, L. Tang, G.M. Zeng, Y.C. Deng, Y.N. Liu, L.L. Wang, Y.Y. Zhou, Z. Guo, Z. Guo, J.J. Wang, C. Zhang, Atomic scale g-C_3N_4/Bi_2WO_6 2D/2D heterojunction with enhanced photocatalytic degradation of ibuprofen under visible light irradiation, Appl. Catal. B 209 (2017) 285–294.

[46] Z.X. Xu, J. Liu, X.H. Wu, B. Huang, X.J. Pan, Nonmonotonic responses to low doses of xenoestrogens: A review. Environ, Environ. Res. 155 (2017) 199–207.

[47] Q.X. Liu, C.M. Zeng, L.H. Ai, Z. Hao, J. Jiang, Boosting visible light photoreactivity of photoactive metal-organic framework: designed plasmonic Z-scheme Ag/AgCl@MIL-53-Fe, Appl. Catal. B 224 (2018) 38–45.